

# CSST-PSFNet: A Point Spread Function Reconstruction Model for the CSST Based on Deep Learning

PEIPEI WANG,<sup>1,2</sup> PENG WEI,<sup>1,2</sup> CHAO LIU,<sup>1,2,3,4</sup> RUI WANG,<sup>1,2</sup> FENG WANG,<sup>5,6</sup> AND XIN ZHANG<sup>1,2</sup>

<sup>1</sup>National Astronomical Observatories, Chinese Academy of Sciences, Beijing 100101, People's Republic of China

<sup>2</sup>School of Astronomy and Space Science, University of Chinese Academy of Sciences, Beijing 100049, People's Republic of China

<sup>3</sup>Institute of Frontiers in Astronomy and Astrophysics, Beijing Normal University, Beijing, 100875, China

<sup>4</sup>Zhejiang Lab, Hangzhou, Zhejiang, 311121, China

<sup>5</sup>Center For Astrophysics, Guangzhou University, Guangzhou, Guangdong 510006, People's Republic of China

<sup>6</sup>Great Bay Center, National Astronomical Data Center, Guangzhou, Guangdong 510006, People's Republic of China

## ABSTRACT

This paper presents CSST-PSFNet, a deep learning method for high-fidelity point spread function (PSF) reconstruction developed for the Chinese Space Station Survey Telescope (CSST). The model integrates a residual neural network, a lightweight Transformer architecture, and a variational latent representation to address key challenges in CSST imaging, including severe PSF undersampling, inter-band variability, and smooth spatial variation across the focal plane. Trained and validated on high-resolution star-PSF pairs generated by the CSST Main Survey Simulator, CSST-PSFNet achieves improved pixel-level accuracy and more precise recovery of shape parameters relevant to weak lensing compared to widely used PSFEx. On both the standard test dataset and a blurred dataset representing the upper bound of expected on-orbit PSF degradation, the model achieves a size residual precision below 0.005 and an ellipticity residual precision below 0.002. A weak-label adaptation experiment further shows that the model can recover PSFEx-level performance when the true PSF is unknown, demonstrating robustness in controlled degradation scenarios and weak-label adaptation experiments. These results indicate that CSST-PSFNet provides a flexible and extensible framework for future on-orbit PSF calibration in large-scale CSST surveys, with potential applications in weak-lensing cosmology and precision astrophysical measurements.

**Keywords:** Astronomy image processing (2306) — Space telescopes (1547) — Deep learning (1938) — Deconvolution (1910)

## 1. INTRODUCTION

Over the past few decades, space-based observatories have revolutionized our exploration of the cosmos, opening an unprecedented window into the Universe that ground-based telescopes cannot fully replicate. By operating beyond Earth's atmosphere, these instruments eliminate distortions caused by atmospheric turbulence, enabling stable, diffraction-limited imaging with unparalleled clarity and precision. Iconic space telescopes such as *the Euclid Telescope* (Euclid)(Mellier et al. 2025), *the James Webb Space Telescope* (JWST)(Treu et al. 2022; Paris et al. 2023; Bergamini et al. 2023), and *the Nancy Grace Roman Space Telescope* (Roman)(Spergel et al. 2015; Akeson et al. 2019) have played a pivotal role in the advancement of astronomical research, delivering groundbreaking insights into galaxy formation and evolution, the growth of cosmic structures, the nature of dark energy and dark matter, and the origins of the Universe itself. These advances underscore the critical importance of space telescope development in pushing the boundaries of human knowledge and fostering interdisciplinary collaborations.

The *Chinese Space Station Survey Telescope* (CSST) is a next-generation space survey mission in China designed to perform a ten-year optical and near-ultraviolet imaging and slitless spectroscopic survey while co-orbiting with

the Chinese Space Station (Collaboration et al. 2025; Zhan 2021). With a 2-meter off-axis three-mirror anastigmat (TMA) optical system and an instantaneous field of view of approximately  $1.1 \text{ deg}^2$ , CSST aims to conduct a wide and deep survey of  $\sim 17,500 \text{ deg}^2$ , enabling precision cosmology through weak gravitational lensing, galaxy clustering, and photometric redshift measurements. Its focal plane consists of 30 detectors totaling 2.6 billion pixels, with an angular scale of  $0.074''$  per pixel and a nominal image quality of  $R_{\text{EE80}} < 0.15''$ , meaning that 80% of the point-source energy is enclosed within roughly two pixels. Eighteen CCDs are dedicated to seven broad-band photometric channels ( $NUV$ ,  $u$ ,  $g$ ,  $r$ ,  $i$ ,  $z$ ,  $y$ ), while twelve CCDs serve three slitless spectroscopic channels ( $GU$ ,  $GV$ ,  $GI$ ), covering 255–1000 nm.

The configuration of CSST enables high-resolution imaging of billions of galaxies and stars, but it also presents significant challenges for image calibration and point spread function (PSF) modeling. First, the detectors are severely undersampled, with each stellar image spanning only about 1.5–2 pixels across its core (compared to finer sampling in missions like HST), which limits the direct recovery of high-frequency structures. Second, the large multi-CCD focal plane, covering seven photometric bands, exhibits noticeable differences between the CCD PSF due to optical alignment and wavelength-dependent effects. Third, even within a single CCD, the PSF varies smoothly but significantly with position due to residual optical aberrations and field-dependent distortions.

Achieving precise modeling of the Point Spread Function (PSF) is crucial to maximize the scientific capabilities of the CSST, given the complex instrumental challenges discussed earlier. Accurate PSF characterization is essential for the CSST’s ability to make milliarcsecond-level astrometric measurements. Any shift in the PSF-induced centroids can bias the estimates of proper motion and parallax (Nie et al. 2025). Moreover, precise PSF modeling is indispensable for key cosmological objectives of the CSST, such as studying weak gravitational lensing and large-scale structures based on photometric redshifts (Gong et al. 2019, 2025; Cao et al. 2018). During weak lensing analyses, gravitational shear signals cause galaxy shape distortions at the percent level (Bartelmann & Schneider 2001). These distortions can be comparable to or even lower than the artificial ellipticities introduced by the instrumental PSF (Kaiser et al. 1995). Consequently, inaccuracies in PSF estimation can introduce biases, such as underestimating shear signals or miscalibrating flux measurements, thereby compromising the telescope’s ability to probe dark energy parameters with a targeted precision of better than 1% or to map the large-scale structure of the Universe across cosmic epochs. Furthermore, with the CSST’s ambitious survey objectives—imaging billions of galaxies at sub-arcsecond resolution over a decade and processing a 2.6 billion-pixel focal plane across multiple bands—the demand for efficient, scalable PSF reconstruction methods becomes paramount, especially in the era of big data astronomy.

PSF modeling is a long-standing challenge in modern optical telescope data processing, and significant progress has been made. PSF modeling techniques have evolved from analytical models based on physical principles to data-driven and deep learning methods. Early parametric models, such as *TinyTim* (Krist 1993) and the effective formalism of PSF (*ePSF*) (Anderson & King 2000; Anderson & King 2006), provided interpretable optical representations but lacked the flexibility to describe complex field-dependent variations. Data-driven methods, such as Resolved Component Analysis (RCA) (Ngolè et al. 2016) and *PSFEx* (Bertin 2011), enhance adaptability by directly learning PSF variations from stellar images. In contrast, hybrid models such as *WaveDiff* (Liaudat et al. 2023) integrate optical priors into differentiable frameworks for end-to-end calibration. In recent years, deep learning has emerged as a powerful alternative for PSF reconstruction, offering strong representational capacity for non-linear and high-dimensional dependencies. Convolutional and encoder–decoder networks can directly infer high-fidelity PSFs from undersampled stellar images, outperforming classical interpolation techniques in both precision and generalization (Jia et al. 2020, 2021; Lanusse et al. 2021). Generative and variational architectures further enable unsupervised learning of PSF manifolds and physical consistency by coupling latent representations with optical constraints (Carney et al. 2024; Ni et al. 2024; Bai et al. 2025).

Despite substantial advances in PSF modeling techniques, ranging from traditional parametric approaches to sophisticated deep learning frameworks, directly applying these existing methods to the CSST presents significant challenges. CSST’s unique instrumental characteristics, including severe undersampling where stellar images span only 1.5–2 pixels, pronounced inter- and intra-CCD PSF variations due to multi-band observations, and optical aberrations, demand tailored solutions that account for these specifics. Conventional models often assume well-sampled data or simpler optical systems, leading to suboptimal performance in capturing the non-analytic, wavelength-dependent, and field-dependent PSF structures inherent to CSST. Moreover, these methods typically depend on image stacking and polynomial fitting across a large number of stellar samples to achieve adequate precision, making them inefficient and data-hungry. Together, these challenges underscore the need for more flexible and data-driven approaches. Deep learning offers a

powerful framework for this purpose, capable of generalizing spatial and instrumental correlations and achieving high reconstruction accuracy even with limited stellar samples.

In this work, we present **CSST-PSFNet**, a conditioned deep generative model for high-fidelity PSF reconstruction. The paper is organized as follows. Section 2 describes the simulated datasets and preprocessing procedures. Section 3 introduces the model architecture, training setup, and evaluation metrics. Section 4 compares **CSST-PSFNet** with **PSFEx** on both standard and in-orbit degradation test sets. Section 5 discusses potential strategies for adapting the model when the true orbit PSF is unknown. Finally, Section 6 concludes the paper.

## 2. DATA PREPARATION

All simulated datasets are generated using the CSST Main Survey Simulator (`csst_msc_sim`)<sup>7</sup>, an end-to-end image simulation framework built upon `GalSim` (Rowe et al. 2015) that incorporates the latest CSST optical design, detector characteristics, and survey configuration (Wei et al. 2025). The simulator renders multi-band stellar images by convolving intrinsic source profiles with wavelength-dependent PSFs while modeling instrumental effects such as field distortion, pixel integration, and charge diffusion. In `csst_msc_sim`, the optical PSF library is derived from the opto-mechanical-thermal (OMT) model of Ban et al. (2022, 2025), covering both static (e.g., fabrication, alignment, surface figure, CCD planarity) and dynamic aberrations (e.g., thermal drift, vibration, pointing jitter). For each of the 18 photometric CCDs, PSFs are precomputed on a  $30 \times 30$  spatial grid across four wavelength sub-bands per filter, interpolated to arbitrary coordinates, and combined via throughput weighting. Each rendered stellar image is linked to its PSF through a unique `obj_id` in the output catalog. In all datasets, the PSFs generated by the CSST simulator are used exclusively as ground-truth supervision in the loss function and are not provided to the network as input features.

NGC 2298 has been designated as one of the primary on-orbit calibration targets for CSST and will be observed using a multi-exposure dither strategy to ensure complete focal plane coverage. **DATASET 1** is constructed from simulated observations of this field, which was identified as suitable owing to its favorable stellar density, negligible bright-star contamination, low extinction, and stable visibility (Ling et al. 2026). By replicating the planned calibration observations, we ensure that **CSST-PSFNet** learns from data representative of actual on-orbit conditions.

The simulated observations are centered at  $RA=102.2451^\circ$  and  $Dec=-36.0053^\circ$ , providing full coverage across all 18 photometric CCDs. As shown in Figure 1, the CSST focal plane has a fixed multi-band layout with the central six CCDs corresponding to the *NUV* and *u* filters. With this pointing, the NGC 2298 core projects primarily between CCD-13 and CCD-18, such that only these two CCDs directly sample the densest cluster region, while the remaining CCDs probe less crowded areas with more uniform stellar distributions. For an old, metal-poor globular cluster such as NGC 2298, only a small fraction of stars emit significant flux at short wavelengths, intrinsically limiting detectable sources in the *NUV/u* bands.

Source detection and stamp extraction are performed using Source Extractor (Bertin & Arnouts 1996). Stars are selected based on `SNR_WIN`, which represents the signal-to-noise ratio measured within a fixed window centered on the stellar centroid, and the `FWHM` (full width at half maximum). We apply the criteria  $50 \leq \text{SNR\_WIN} \leq 300$  and  $0 \leq \text{FWHM} \leq 4$  pixels and exclude sources flagged as blended or deblended to ensure all samples represent isolated point sources. This yields 17,968 stellar samples in simulated NGC 2298, randomly partitioned into 14,240 training samples (80%) and 3,728 validation samples (20%). Each sample consists of a  $32 \times 32$  stellar cutout, the corresponding  $64 \times 64$  ground truth PSF stamp, and metadata including CCD identifier (`iCCD`) and focal-plane coordinates ( $x, y$ ).

To enable controlled evaluation, **DATASET 2** was generated using the same simulator configuration but an independent source catalog. Stars were placed on the  $30 \times 30$  PSF grid nodes on each CCD, with flux scaled to achieve  $S/N \approx 200$  in the *g* band and uniform brightness enforced. This dataset contains approximately 900 samples per CCD and serves as the nominal benchmark for assessing PSF reconstruction accuracy, exhibiting the expected wavelength-dependent morphology (Figure 1).

Finally, **DATASET 3** was constructed by convolving each PSF in **DATASET 2** with an isotropic Gaussian kernel, introducing a controlled and simplified PSF broadening scenario. This experiment is intended to represent moderate, approximately isotropic degradation dominated by mild defocus, rather than to capture arbitrary on-orbit PSF perturbations. The kernel width of  $\sigma = 0.5$  pixels is chosen based on OMT simulations of the CSST, which is consistent with typical OMT-predicted defocus amplitudes. The dataset preserves the same sample count and structure as **DATASET**

<sup>7</sup> [https://csst-tb.bao.ac.cn/code/csst-sims/csst\\_msc\\_sim](https://csst-tb.bao.ac.cn/code/csst-sims/csst_msc_sim).

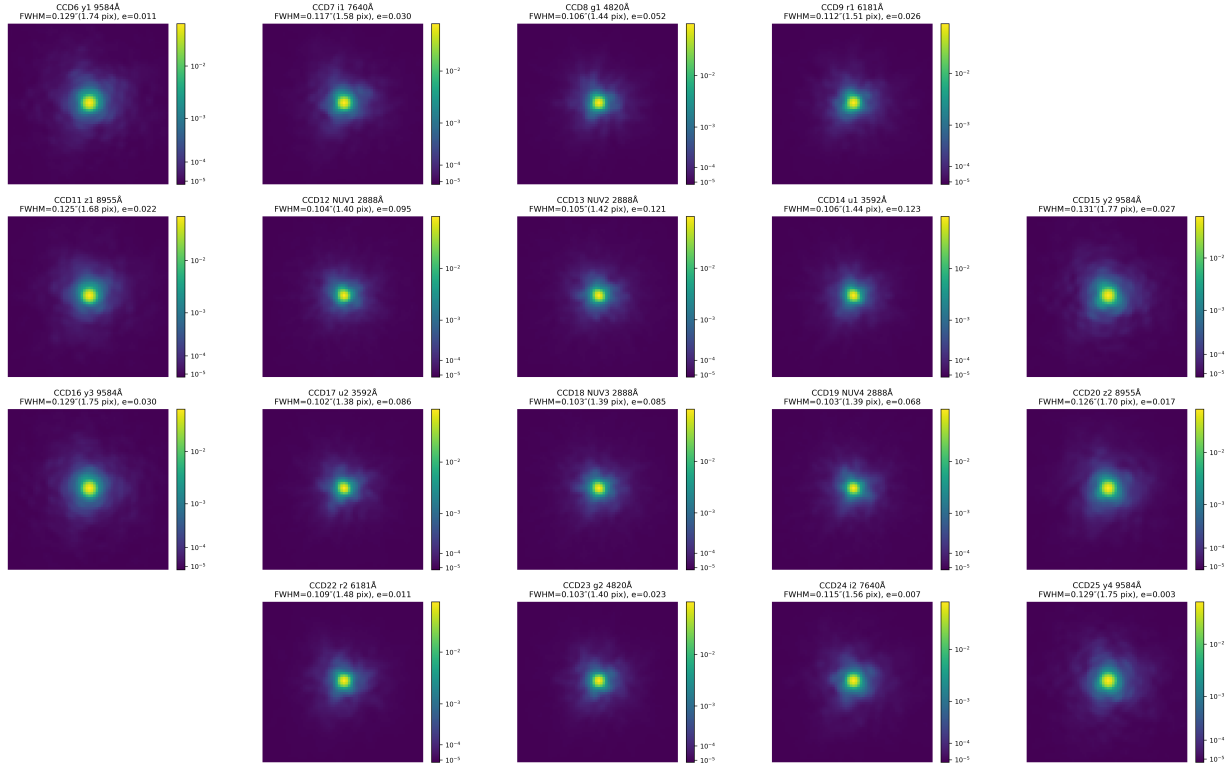


**Figure 1.** Representative PSFs at the detector center from all 18 photometric CCDs in DATASET 2. For each CCD, the PSF is extracted from the ground-truth spatial PSF field of DATASET 2 at the grid position closest to the CCD center. The labels above each subfigure indicate the CCD index, photometric band, effective wavelength, FWHM, and PSF ellipticity  $e$ . The full spatially varying PSF fields in DATASET 2 are used as the ground truth for evaluating the corresponding PSF reconstruction results. The color scale represents the normalized PSF intensity and is displayed on a logarithmic scale with logarithmically spaced color-bar ticks, highlighting both the PSF core and low-intensity wing structures. Note that the displayed PSFs are shown on the  $2\times$  upsampled grid ( $0.037''/\text{pixel}$ ) for visualization, but the quoted FWHM values are reported in native CSST pixels ( $0.074''/\text{pixel}$ ) for consistency with instrument specifications; equivalently, the FWHM on the displayed grid is twice the quoted value.

2, while exhibiting broader and more symmetric PSFs consistent with this controlled degradation setting. Figure 2 presents the Gaussian-blurred counterparts of the PSFs shown in Figure 1, illustrating the expected increase in FWHM and the corresponding reduction in ellipticity resulting from isotropic convolution.

### 3. MODEL DESIGN AND MODELING

#### 3.1. Model Design

We propose CSST-PSFNet, a Transformer-augmented conditional variational encoder–decoder specifically designed for instrument-aware PSF super-resolution across the CSST focal-plane array, as illustrated in Figure 3. The network maps a low-resolution  $32 \times 32$  stellar cutout  $\mathbf{x}$ , together with the CCD index (iCCD) and normalized focal-plane coordinates  $\mathbf{p}$ , to a high-fidelity  $64 \times 64$  PSF reconstruction  $\hat{\mathbf{y}}$ .

The encoder compresses the stellar input through three residual convolutional modules that capture both the PSF core intensity and diffraction-ring morphology. A lightweight attention module performs channel–spatial reweighting at the bottleneck scale, enhancing feature coherence and emphasizing physically meaningful structures. Positional and detector conditions are embedded jointly to provide instrument-aware contextual information. The encoded features are tokenized and passed through a multi-layer Transformer encoder that models global dependencies across spatial and detector domains. A variational head projects the encoder output into the parameters of a diagonal Gaussian distribution, from which a latent code  $\mathbf{z}$  is sampled using the reparameterization trick.

The decoder performs conditional reconstruction by integrating the latent code  $\mathbf{z}$  with positional and detector context. Through cross-attention, the Transformer decoder retrieves PSF features consistent with both spatial position

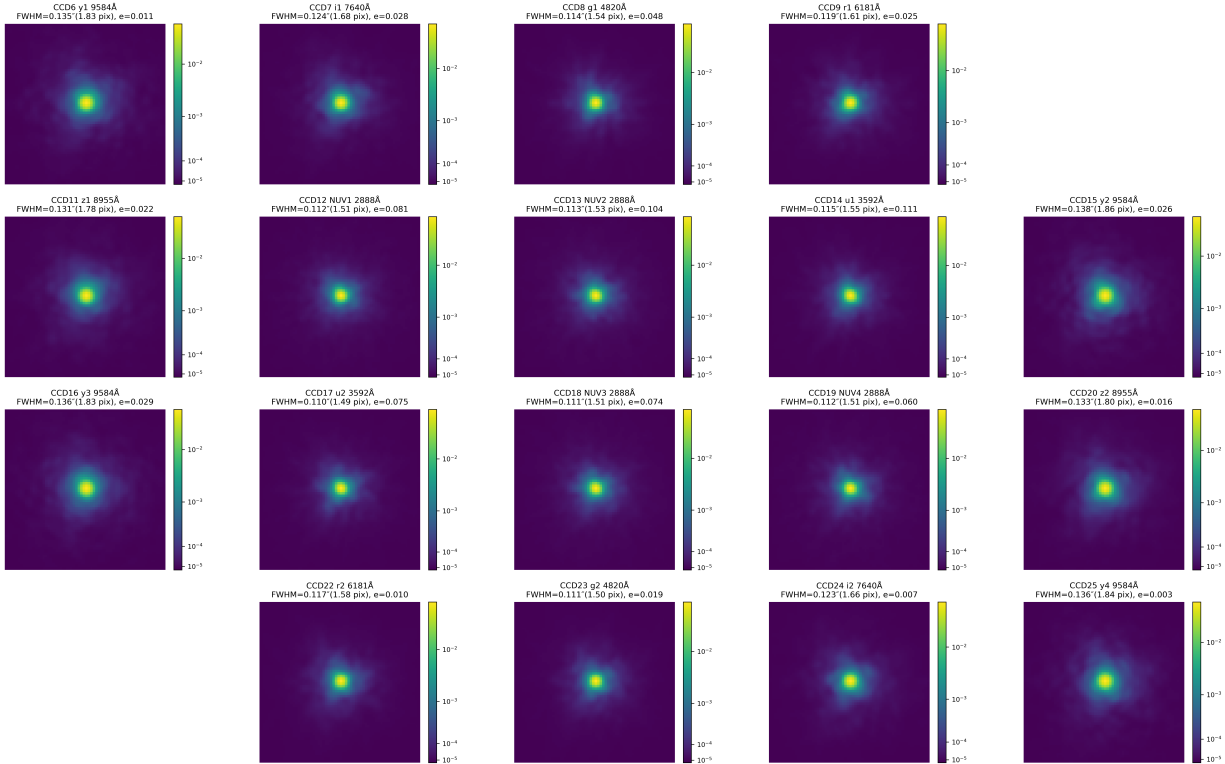


**Figure 2.** Same as Figure 1, but for DATASET 3. Representative PSFs at the detector center are extracted from the ground-truth spatial PSF fields of DATASET 3 and used to assess the PSF reconstruction performance under this dataset. The color scale represents the normalized PSF intensity and is shown on a logarithmic scale with logarithmically spaced color-bar ticks, enabling visualization of both the PSF core and faint wing structures.

and CCD-specific properties. The decoded representation is progressively upsampled through a lightweight reconstruction stack to produce the  $64 \times 64$  high-resolution PSF. Upsampling is implemented using sub-pixel convolution (PixelShuffle), which mitigates aliasing and preserves structural continuity. A shallow convolutional head maps the final feature maps into a single-channel PSF image. Non-negative intensities are enforced by a sigmoid activation at the output layer. The reconstructed PSF is then normalized by its total flux on a per-sample basis to ensure unit flux.

Accurate PSF reconstruction under the severe undersampling of CSST requires the network to preserve both local morphological details and global photometric consistency. The residual and attention modules provide strong local representation capability, while the Transformer encoder captures long-range dependencies and detector-level correlations. To represent smooth spatial variations and inter-detector differences, the positional encoder transforms focal-plane coordinates  $(x, y)$  into learnable geometric features, and the CCD embedding encodes detector-specific statistics.

The model is optimized with a composite loss that includes pixel reconstruction and variational regularization. Let  $\hat{\mathbf{P}}, \mathbf{P} \in \mathbb{R}^{H \times W}$  denote the reconstructed and ground-truth PSFs, respectively. The total loss is

$$\mathcal{L}_{\text{total}} = \lambda_{\text{rec}} \mathcal{L}_{\text{rec}} + \lambda_{\text{kld}} \mathcal{L}_{\text{kld}}. \quad (1)$$

Reconstruction loss measures the fidelity at the pixel-level between  $\hat{\mathbf{P}}$  and  $\mathbf{P}$ ,

$$\mathcal{L}_{\text{rec}} = \|\hat{\mathbf{P}} - \mathbf{P}\|_F^2 = \sum_{u=1}^H \sum_{v=1}^W (\hat{P}_{uv} - P_{uv})^2. \quad (2)$$

The variational regularization term constrains the latent posterior  $q(\mathbf{z}|\mathbf{x}) = \mathcal{N}(\boldsymbol{\mu}, \text{diag}(\boldsymbol{\sigma}^2))$  toward the unit Gaussian prior  $p(\mathbf{z}) = \mathcal{N}(\mathbf{0}, \mathbf{I})$  via the Kullback–Leibler divergence,

$$\mathcal{L}_{\text{kld}} = \frac{1}{2} \mathbb{E} [\|\boldsymbol{\mu}\|^2 + \|\boldsymbol{\sigma}\|^2 - \log \boldsymbol{\sigma}^2 - 1]. \quad (3)$$

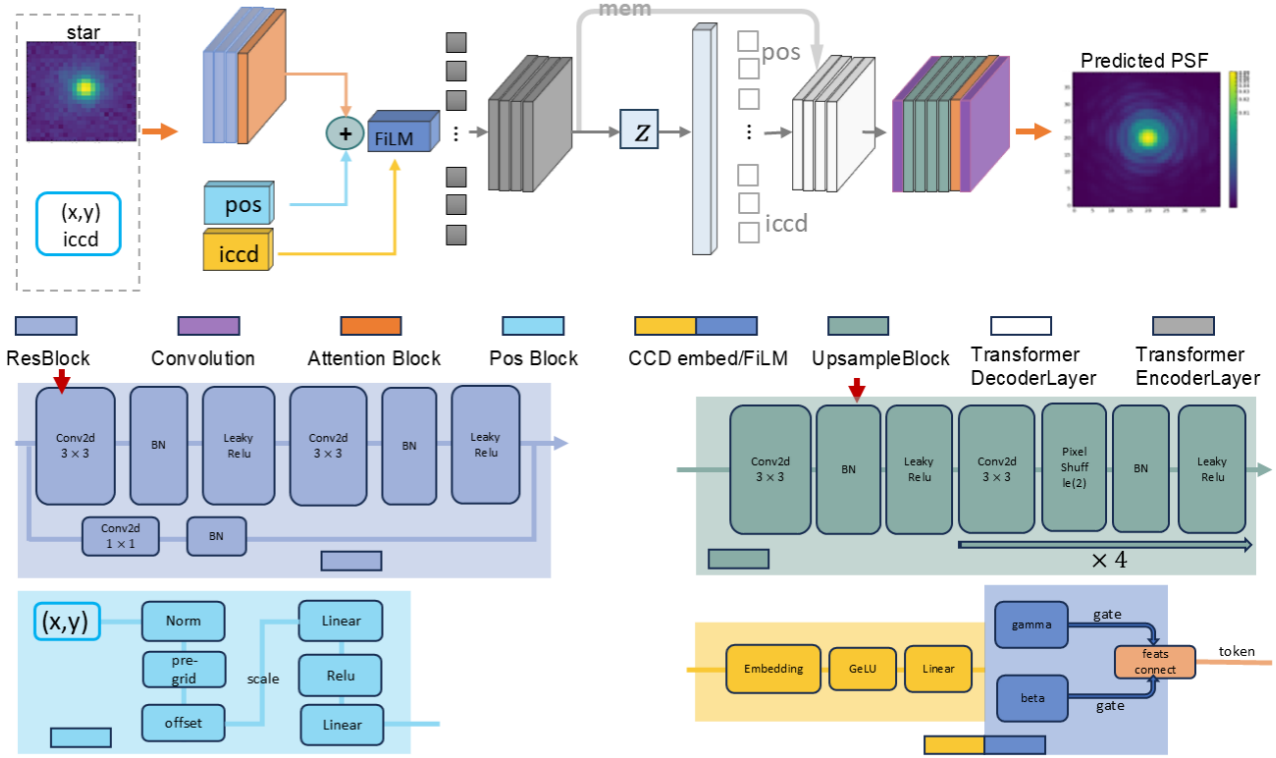


**Figure 3.** Architecture of CSST-PSFNet, integrating convolutional encoding, CCD/position conditioning, and Transformer-based dual-query decoding for PSF reconstruction. Bottom: module details of ResBlock, Pos Block, CCD embed/FiLM, and UpsampleBlock.

Its weight  $\lambda_{kld}$  is linearly annealed during the warm-up phase,

$$\lambda_{kld}(t) = \lambda_{\min} + (\lambda_{\max} - \lambda_{\min}) \min\left(\frac{t}{T_{\text{ramp}}}, 1\right), \quad (4)$$

where  $t$  is the epoch index and  $(\lambda_{\min}, \lambda_{\max}, T_{\text{ramp}})$  are the annealing parameters.

### 3.2. Modeling

CSST-PSFNet is trained using the AdamW optimizer with an initial learning rate of  $1 \times 10^{-4}$  and a weight decay of  $1 \times 10^{-5}$ . A five-epoch linear warm-up is followed by a cosine decay schedule that gradually reduces the learning rate to 1% of its initial value. Training proceeds for up to 200 epochs with early stopping (patience of 20), and convergence is typically reached at epoch 40. We adopt a batch size of 16, employ mixed-precision training, and apply gradient clipping at 0.5 to ensure stable optimization. We verified that moderate variations of learning rate and latent dimension do not significantly affect the reconstruction metrics. The training objective combines a reconstruction term and a KLD regularization term, with weights  $\lambda_{\text{rec}} = 1.0$  and  $\lambda_{\text{kld}} = 1.0$ , respectively. All experiments are conducted on a Linux server equipped with an NVIDIA A100 GPU (40 GB). The implementation is based on PyTorch and is executed in a CUDA 12.2 runtime environment.

DATASET 1 is split into 14,240 training samples (about 890 batches) and 3,728 samples (about 223 batches) for validation. Both evaluation datasets, DATASET 2 and DATASET 3, comprise approximately 860-900 stellar samples per CCD over all 18 imaging CCDs. Whereas DATASET 2 serves as the nominal reference set, DATASET 3 augments it by applying an isotropic Gaussian kernel to each PSF, producing a systematically broadened counterpart for testing robustness to realistic on-orbit perturbations.

### 3.3. Evaluation Metrics and Validation

To quantitatively evaluate the fidelity of PSF reconstruction, we adopt two complementary categories of metrics: (1) pixel-level image fidelity indices, which measure the similarity between reconstructed and reference PSF images at

the pixel scale, and (2) shear-related shape metrics, which probe the recovery of PSF size and ellipticity—quantities that are of central importance for weak-lensing cosmology.

### 3.3.1. Pixel-level metrics

Pixel-level metrics provide a direct evaluation of the similarity between the reconstructed PSF image  $I_{\text{rec}}$  and the ground-truth PSF  $I_{\text{true}}$ . We consider three complementary measures:

1. **Root Mean Square Error (RMSE)**; RMSE quantifies the average pixel-wise deviation between two images and is defined as

$$\text{RMSE} = \sqrt{\frac{1}{N} \sum_{i=1}^N (I_{\text{rec},i} - I_{\text{true},i})^2}, \quad (5)$$

where  $N$  is the number of pixels. It is reported in the same units as the image intensity and reflects the typical reconstruction error per pixel. In PSF modeling, a smaller RMSE indicates closer agreement with the reference, which serves as a baseline measure of pixel-level reconstruction fidelity.

2. **Peak Signal-to-Noise Ratio (PSNR)**. PSNR expresses the reconstruction quality on a logarithmic scale:

$$\text{PSNR} = 20 \log_{10} \left( \frac{I_{\text{max}}}{\sqrt{\text{MSE}}} \right), \quad \text{MSE} = \frac{1}{N} \sum_{i=1}^N (I_{\text{rec},i} - I_{\text{true},i})^2, \quad (6)$$

where  $I_{\text{max}}$  is the maximum intensity in the ground truth PSF. Higher PSNR values indicate superior fidelity to the reference PSF.

3. **Structural Similarity Index (SSIM)**. SSIM measures image similarity in terms of luminance, contrast, and structural information (Wang et al. 2004; Avanaki 2009):

$$\text{SSIM}(x, y) = \frac{(2\mu_x\mu_y + C_1)(2\sigma_{xy} + C_2)}{(\mu_x^2 + \mu_y^2 + C_1)(\sigma_x^2 + \sigma_y^2 + C_2)}, \quad (7)$$

where  $\mu_x, \mu_y$  are the local means,  $\sigma_x^2, \sigma_y^2$  are the variances and  $\sigma_{xy}$  is the covariance. The constants  $C_1$  and  $C_2$  are included to ensure numerical stability in low-intensity regions of PSF images, where the local mean and variance can approach zero. SSIM ranges from 0 to 1, with higher values denoting greater structural similarity.

### 3.3.2. Shear-related metrics

Besides pixel-level fidelity, weak-lensing science places stringent requirements on the recovery of PSF size and shape, since residual errors in these quantities propagate directly into multiplicative and additive shear biases (Paulin-Henriksson et al. 2008, 2009). Therefore, we employ the adaptive-moment formalism (Hirata & Seljak 2003) to assess the precision of reconstructed PSFs. In this approach, the surface brightness distribution  $I(x, y)$  is characterized by its adaptive second moments, measured with an elliptical Gaussian weight function, iteratively matched to the object profile.

The adaptive quadrupole moments are defined as

$$Q_{ij} = \frac{\int (x_i - \bar{x}_i)(x_j - \bar{x}_j) I(x, y) W(x, y) dx dy}{\int I(x, y) W(x, y) dx dy}, \quad i, j \in \{x, y\}, \quad (8)$$

where  $W(x, y)$  is the elliptical Gaussian weight matched and  $(\bar{x}_i, \bar{x}_j)$  is the centroid. From these moments, the effective PSF size is given by

$$R^2 = Q_{xx} + Q_{yy}, \quad (9)$$

and the ellipticity components are expressed as

$$e_1 = \frac{Q_{xx} - Q_{yy}}{Q_{xx} + Q_{yy}}, \quad e_2 = \frac{2Q_{xy}}{Q_{xx} + Q_{yy}}, \quad e = \sqrt{e_1^2 + e_2^2}. \quad (10)$$

We define the size and ellipticity deviation as follows:

$$\delta R^2 / R^2 = \frac{R_{\text{rec}}^2 - R_{\text{true}}^2}{R_{\text{true}}^2}, \quad \delta e = e_{\text{rec}} - e_{\text{true}}, \quad (11)$$

where the subscripts 'rec' and 'true' refer to measurements from the reconstructed PSFs (either PSFEx or CSST-PSFNet) and the corresponding ground-truth PSFs, respectively. Heymans et al. (2005) modeled the time and position dependent variation of the PSF in the absence of a known true PSF by fitting the stellar ellipticity field across the HST/ACS images, and evaluated the model accuracy using the root-mean-square (RMS) of the stellar-model ellipticity residuals. In this work, since the simulated datasets provide the theoretical PSF as ground truth, we can directly quantify the reconstruction accuracy by computing the standard deviations of the residuals in both shape and size parameters:

$$\sigma(\delta e) = \text{std}(\delta e), \quad \sigma(\delta R^2/R^2) = \text{std}\left(\frac{\delta R^2}{R_{\text{true}}^2}\right).$$

These standard deviation metrics are numerically equivalent to the stellar residual RMS used in weak-lensing PSF studies (e.g., Heymans et al. 2005) and provide a proxy to the additive and multiplicative shear calibration biases potentially introduced by PSF reconstruction errors.

#### 4. PERFORMANCE ANALYSIS

To contextualize the performance of CSST-PSFNet, we adopt PSFEx as a reference baseline. PSFEx is a survey-grade PSF modeling method widely used in weak-lensing studies and validated across major surveys such as HSC (Mandelbaum et al. 2017), DES (Zuntz et al. 2018), and CFIS (Guinot et al. 2022). Working jointly with Source Extractor (Bertin & Arnouts 1996), it constructs spatially varying PSF models from stellar cutouts using a non-parametric formulation (Bertin 2011). Each PSF is expressed as a linear combination of eigen-PSFs derived from singular value decomposition, while the spatial variation of the associated coefficients is captured through smooth low-order polynomials across the focal plane.

In this study, PSFEx is configured with a third-order polynomial spatial model and produces PSFs on a  $2\times$  oversampled grid, which matches the target resolution of CSST-PSFNet. A key methodological distinction is that CSST-PSFNet is trained once on DATASET 1 and applied to all test sets with fixed parameters, whereas PSFEx is re-fitted independently on each dataset, reflecting different operational paradigms. All data preprocessing steps are kept consistent with those used for CSST-PSFNet, ensuring that the comparison isolates modeling performance rather than differences in data handling.

##### 4.1. Quantitative Results on DATASET 2

We begin our comparison with residual maps across the full focal plane. For the same positions shown in Figure 1, Figures 4 and 5 display the residuals of the CSST-PSFNet and PSFEx reconstructions. Both methods reproduce the gross morphology, but their residual patterns differ substantially. PSFEx solutions typically show a bright positive core surrounded by a negative ring (e.g., CCD 6–7, 9, 11, 15–16, 20, 24–25), and in the *NUV* and *u* bands exhibit concentric positive–negative rings, reflecting the difficulty in simultaneously fitting the PSF core and extended wings. In contrast, CSST-PSFNet residuals are typically an order of magnitude smaller ( $\text{RMS} \sim 10^{-5}$  v.s.  $\sim 10^{-4}$  for PSFEx) and do not display such large-scale ring-like artifacts. Instead, they contain only fine, low-amplitude high-frequency structures, indicating that while large-scale residuals are strongly suppressed, small-scale deviations remain. These results highlight the ability of CSST-PSFNet to simultaneously capture the PSF core and wings, a requirement of weak-lensing science.

In addition to visual inspection, we analyzed the spatial distributions of the FWHM and ellipticity residuals throughout the entire focal plane. Figures 6 and 7 show the maps of  $\delta R^2/R^2$  and  $\delta e$  for CSST-PSFNet and for PSFEx. For FWHM (Figures 6a, 7a), CSST-PSFNet maintains deviations within  $\pm 0.5\%$ , with RMS values at the 0.001 level, and shows no coherent large-scale patterns. In contrast, PSFEx reconstructions exhibit strong alternating positive–negative stripe and patch-like structures, with amplitudes reaching several percent. The effect is particularly severe in the *NUV* and *u* bands, where undersampling is strongest in the central six CCDs, and RMS values can reach 0.02. For ellipticity residuals (Figures 6b, 7b), CSST-PSFNet consistently achieves low RMS levels of  $5.6 \times 10^{-4}$  -  $3.1 \times 10^{-3}$  across all CCDs, with spatially uniform distributions and no large-scale artifacts. By contrast, PSFEx frequently exceeds the 0.01 level, with several CCDs in the undersampled *NUV*, *u*, and parts of the *g* band showing saturated residual patches close to the colorbar limits  $\pm 0.02$ , indicating substantial inaccuracies in modeling the anisotropy of the PSF. In general, CSST-PSFNet reduces residuals in both *R* and *e* by at least an order of magnitude compared to PSFEx, achieving more accurate and spatially uniform PSF reconstructions. This improvement is critical for weak-lensing applications, where even percent-level biases in PSF size or ellipticity directly propagate into shear measurement residuals.

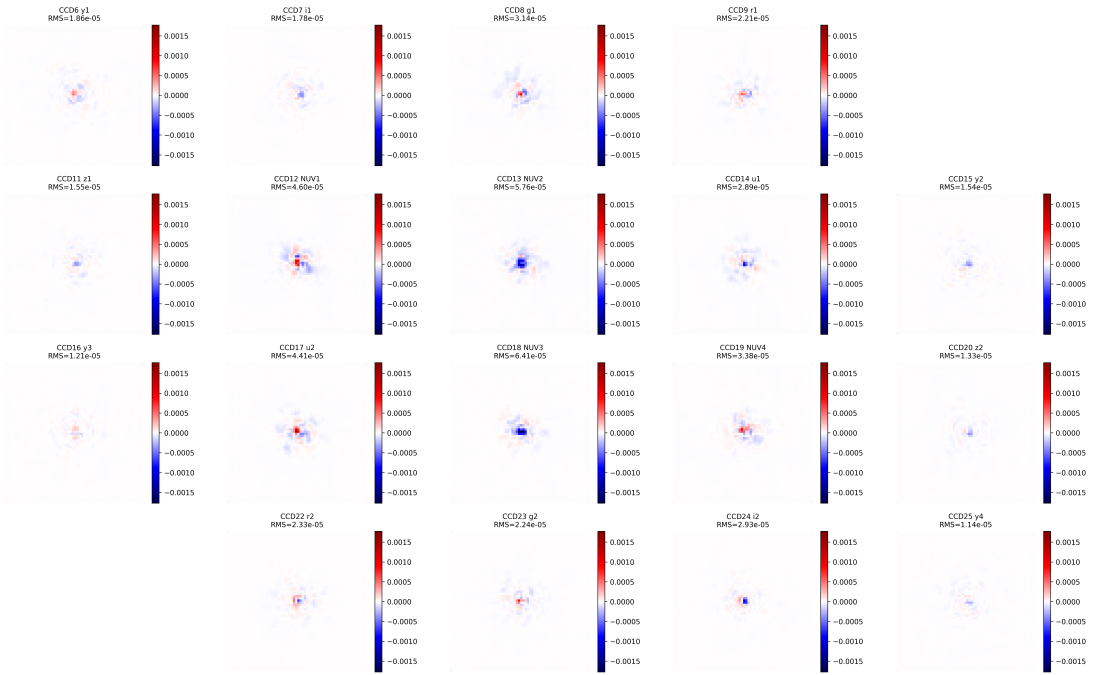


**Figure 4.** Residual maps of the central PSFs reconstructed by CSST-PSFNet for all 18 CCDs on DATASET 2. Compared to the PSFEx results (Figure 5), the model residuals are typically an order of magnitude smaller in RMS ( $\sim 10^{-5}$  versus  $\sim 10^{-4}$ ), and large-scale ring-like artifacts are absent. Only fine high-frequency structures of low amplitude remain, demonstrating the model’s improved ability to capture both PSF cores and wings across the full focal plane.

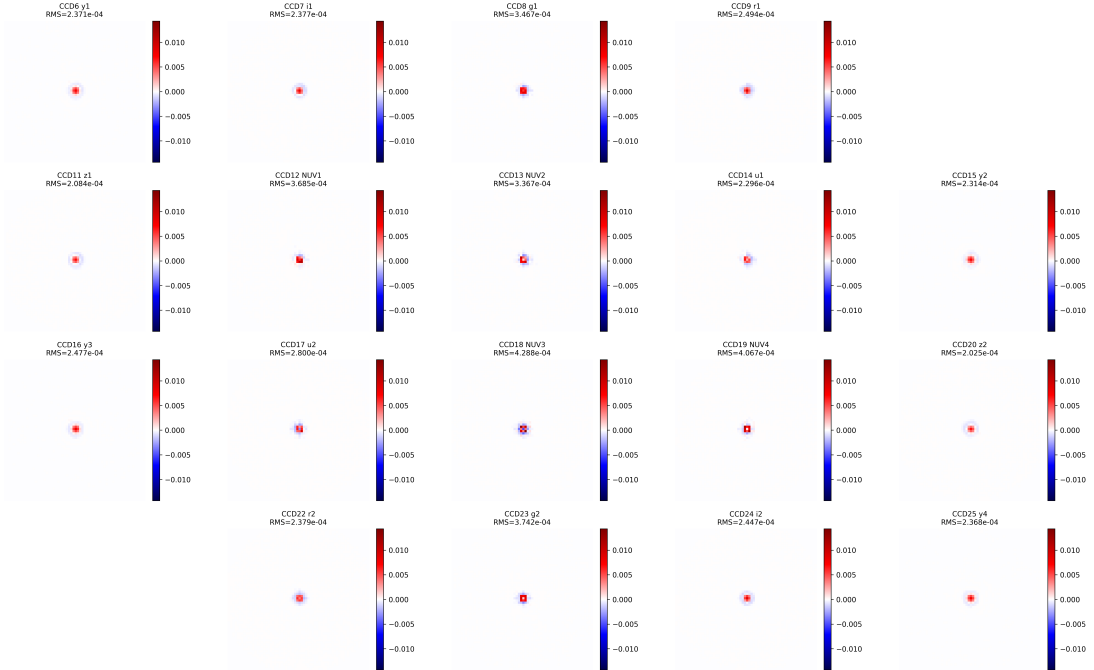


**Figure 5.** Residual maps of the central PSFs reconstructed by PSFEx for all 18 CCDs on DATASET 2, relative to the ground truth PSFs shown in Figure 1. The reconstructions reproduce the overall morphology but leave prominent features, most notably bright central cores (red) surrounded by negative rings (blue). These features indicate difficulties in simultaneously matching both the PSF core and extended wings.

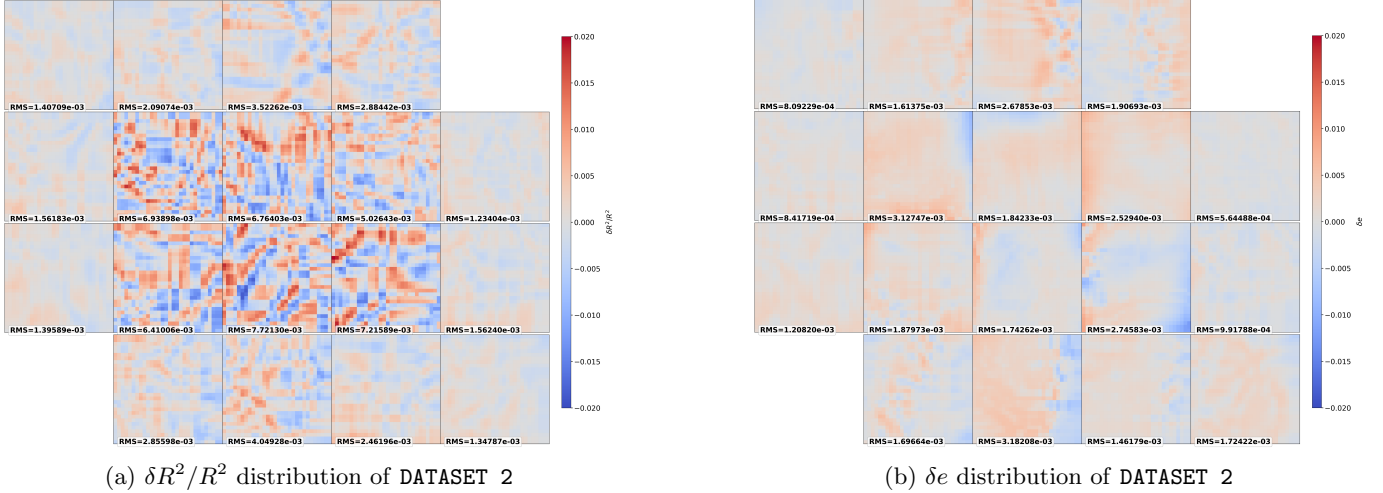


**Figure 6.** Residual distributions of PSF size ( $\delta R^2/R^2$ , panel a) and ellipticity ( $\delta e$ , panel b) across all 18 CCDs for CSST-PSFNet, evaluated on DATASET 2. The residuals remain compact and spatially uniform, with RMS values at the  $10^{-3}$  level and deviations generally confined within  $\pm 0.5\%$  for PSF size and  $\sim 10^{-3}$  for ellipticity. No large-scale coherent artifacts are visible, indicating that CSST-PSFNet accurately captures both PSF size and anisotropy across the focal plane.

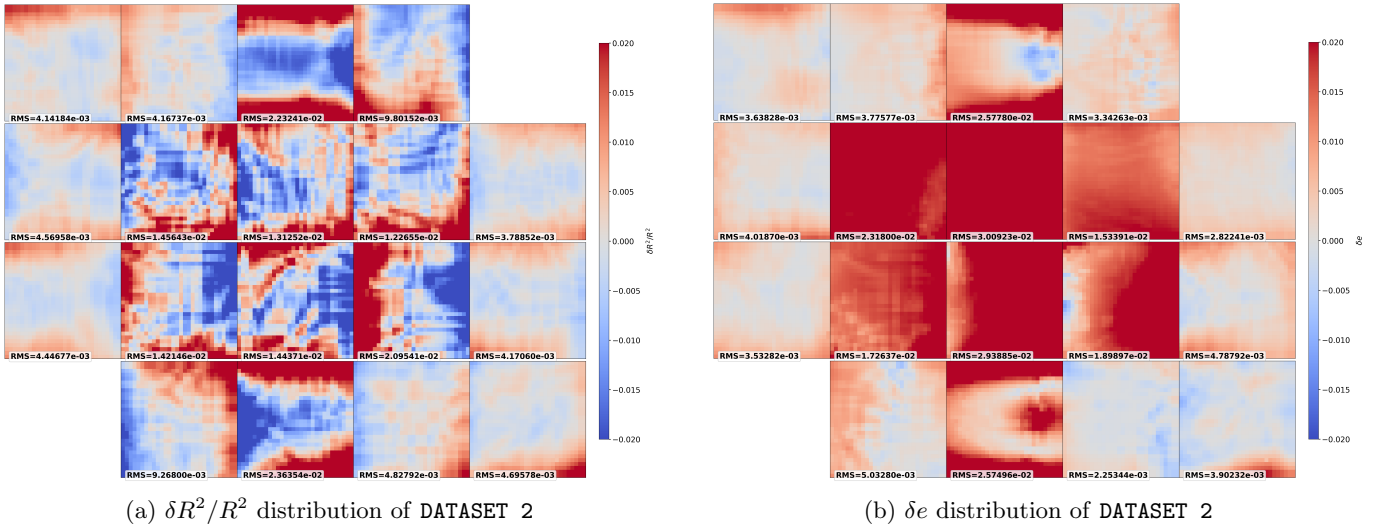


**Figure 7.** Residual distributions of PSF size ( $\delta R^2/R^2$ , panel a) and ellipticity ( $\delta e$ , panel b) across all 18 CCDs for PSFEx, evaluated on DATASET 2. Compared to CSST-PSFNet, PSFEx shows substantially larger residuals: the PSF size residuals exhibit stripe-like and patchy patterns with amplitudes of several percent (RMS up to  $2 \times 10^{-2}$ ), while the ellipticity residuals often exceed the  $10^{-2}$  level and display saturated regions close to the  $\pm 0.02$  limits, particularly in the undersampled *NUV*, *u*, and *g* bands. These results highlight the limitations of PSFEx in capturing spatial variations of PSF morphology.

Table 1 summarizes the pixel-level reconstruction quality. Compared with PSFEx, CSST-PSFNet reduces the RMSE from  $\sim 3 \times 10^{-3}$  to  $\sim 2 \times 10^{-4}$  (a  $\sim 15\times$  improvement, i.e., just over one order of magnitude), while the PSNR increases from 51 to 71. The SSIM values correspondingly move closer to unity, indicating improved structural fidelity. In particular, these gains are observed throughout the spectral range, from the severely undersampled *NUV* and *u* bands to the longer-wavelength *y* band, demonstrating that the proposed method retains superior reconstruction fidelity, irrespective of the level of undersampling. This consistency across bands emphasizes the robustness of CSST-PSFNet, particularly in challenging, undersampled conditions. It reinforces its capability to produce high-quality reconstructions across the full CSST spectral range. In addition, PSFEx requires approximately 4738 seconds to construct the PSF

**Table 1.** Per-band averages of pixel-level reconstruction metrics for PSFEx and CSST-PSFNet evaluated on DATASET 2. Lower RMSE and higher PSNR/SSIM indicate better performance.

Bandpass	PSFEx			Model		
	PSNR	SSIM	RMSE	PSNR	SSIM	RMSE
NUV	47.9108	0.9979	0.0041	67.9715	0.9998	0.0004
u	50.5035	0.9967	0.0030	69.6252	0.9999	0.0003
g	50.8477	0.9962	0.0029	72.4350	0.9999	0.0002
r	53.2417	0.9967	0.0021	72.0391	0.9999	0.0002
i	52.8541	0.9986	0.0022	70.9628	0.9999	0.0002
z	53.2098	0.9986	0.0021	73.9183	0.9999	0.0002
y	53.5175	0.9990	0.0021	73.6150	0.9999	0.0002
Mean	51.5014	0.9978	0.0027	71.3503	0.9999	0.0002

model for the dataset, whereas CSST-PSFNet completes inference in 296 seconds, corresponding to an approximately  $16\times$  reduction in runtime.

#### 4.2. Quantitative Results on DATASET 3

To evaluate the robustness of CSST-PSFNet under realistic on-orbit perturbations, we compare both methods on DATASET 3. Because the applied Gaussian blur suppresses high-frequency structures, the residual maps of PSF reconstruction become less informative, and therefore, our analysis for DATASET 3 focuses on the physically meaningful PSF size and ellipticity residuals.

Figures 8 and 9 present the spatial distributions of the size and ellipticity residuals,  $\delta R^2/R^2$  and  $\delta e$ . DATASET 3 effectively broadens the nominal PSFs, reducing the degree of undersampling and thus mitigating high-frequency discrepancies between the predicted and true PSFs. Nevertheless, PSFEx still exhibits noticeable artificial structures, particularly along the edges of the *NUV*, *u*, *g* bands, revealing its inherent limitations in interpolation-based modeling. In contrast, CSST-PSFNet achieves consistently smaller residuals across all bands and shows no visible artifacts, with the improvement being most pronounced in the severely undersampled blue bands. These results confirm that the proposed model provides more accurate and physically stable PSF reconstructions under on-orbit-like conditions, demonstrating superior robustness and generalization compared to the traditional interpolation approach.

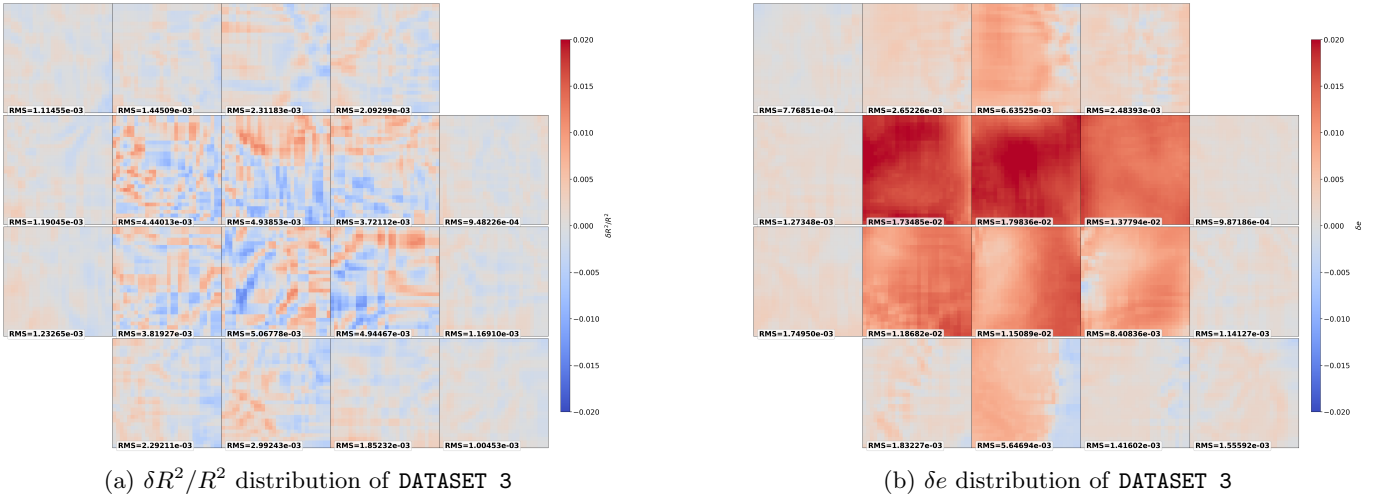


**Figure 8.** Residual distributions of PSF size ( $\delta R^2/R^2$ , panel a) and ellipticity ( $\delta e$ , panel b) across all 18 CCDs for CSST-PSFNet, evaluated on DATASET 3.

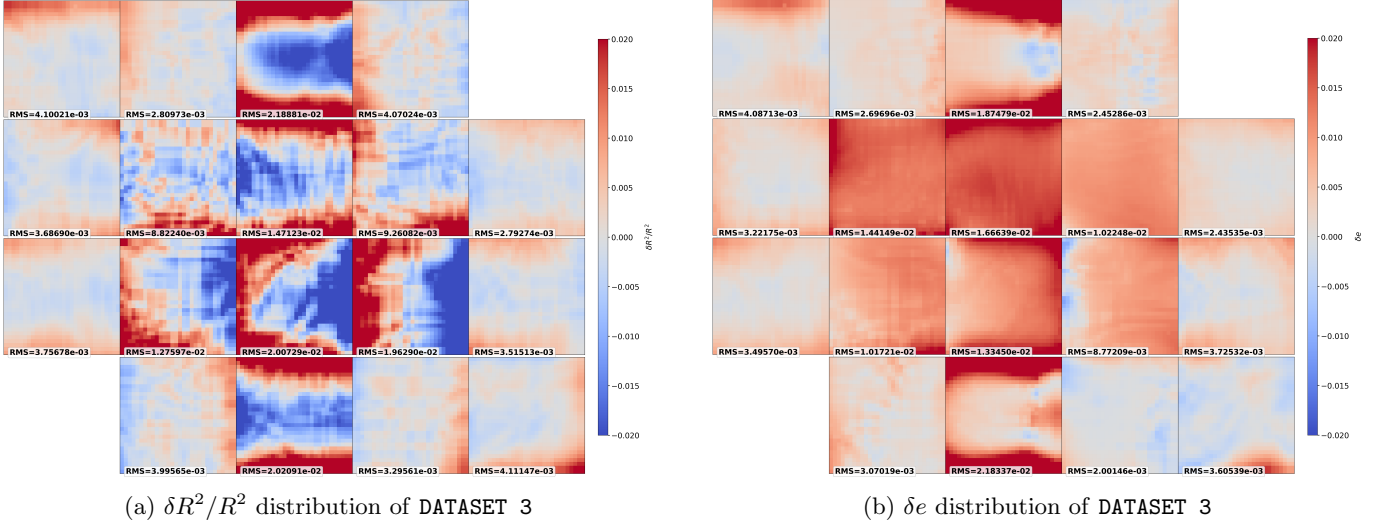


**Figure 9.** Residual distributions of PSF size ( $\delta R^2/R^2$ , panel a) and ellipticity ( $\delta e$ , panel b) across all 18 CCDs for PSFEx, evaluated on DATASET 3.

### 4.3. Cross-band Consistency and Robustness

Figure 10 summarizes the cross-band residual statistics of PSF size and ellipticity for both PSFEx and CSST-PSFNet under DATASET 2 and DATASET 3. Across all photometric bands, CSST-PSFNet exhibits dispersions substantially smaller than those of PSFEx, demonstrating superior cross-band consistency. In terms of PSF size, the dispersion  $\sigma(\delta R^2/R^2)$  for CSST-PSFNet remains below 0.005 in the focal plane and drops to  $\sim 0.002$  in the redder bands, while PSFEx shows significantly higher values, particularly in the blue filters where undersampling is most severe.

After Gaussian broadening, both methods show reduced  $\sigma(\delta R^2/R^2)$ , reflecting the smoothing effect of isotropic convolution on high-frequency structures. For ellipticity, PSFEx shows a uniform decrease in  $\sigma(\delta e)$  across all bands, while CSST-PSFNet exhibits a modest increase in the bluest filters and remains nearly unchanged toward the red. This trend is consistent with the physical impact of Gaussian blurring, which weakens the anisotropic features of sharp blue band PSFs and thus reduces the morphological cues available to the network.

Despite these effects, CSST-PSFNet maintains lower residual dispersions in both  $\sigma(\delta R^2/R^2)$  and  $\sigma(\delta e)$  across all bands and conditions, indicating that the model is more robust in recovering PSF size and anisotropy even under degraded or smoothed observational scenarios.

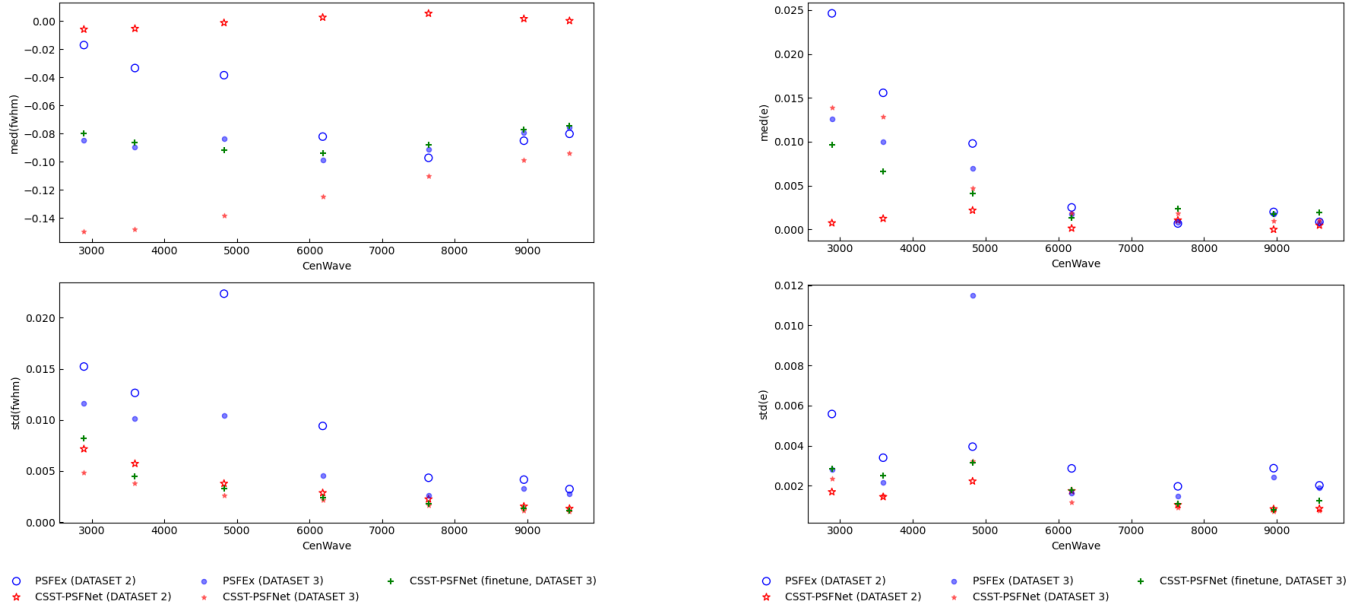


**Figure 10.** Cross-band statistics of PSF reconstruction accuracy grouped by filter central wavelength. The **top panels** show the median residuals of the size ratio  $\delta R^2/R^2$  and the ellipticity components  $\delta e$  across all CCDs in each band. The **bottom panels** present the corresponding dispersions  $\sigma(\delta R^2/R^2)$  and  $\sigma(\delta e)$ , evaluating the stability of the reconstruction. Blue markers denote results from PSFEx, while red markers denote results from CSST-PSFNet. For DATASET 2, results are shown as large open circles (PSFEx) and large open star markers (CSST-PSFNet). For the Gaussian-blurred test set DATASET 3, results are shown as small filled circles (PSFEx) and small filled star markers (CSST-PSFNet). Green plus symbols indicate the performance of CSST-PSFNet on DATASET 3 after fine-tuning with PSFEx-predicted PSFs as weak labels (see Section 5).

## 5. DISCUSSIONS

### 5.1. Weak Supervision, Model Limitations, and Future Calibration

This study evaluates the performance of CSST-PSFNet using high-fidelity simulations generated by the CSST Main Survey Simulator (Wei et al. 2025; Bai et al. 2025). While these simulations incorporate realistic optical modeling, focal-plane geometry, and detector physics, they inevitably represent an idealized approximation of on-orbit conditions. Real observations may exhibit complex instrument-state evolution, time-dependent perturbations (thermal drift, micro-vibrations, detector aging), and unforeseen optical artifacts not fully captured in pre-launch simulations. These limitations necessitate a strategy for model adaptation using real on-orbit data.

To explore adaptation under realistic constraints, we conducted a fine-tuning experiment (Section 4.3, Figure 10) in which PSFEx-estimated PSFs serve as weak supervisory labels. After fine-tuning, the residuals in median  $\delta R^2/R^2$  (particularly prominent in blue bands) reduce toward PSFEx levels while maintaining lower random scatter. This result indicates that CSST-PSFNet can align with PSFEx-level reconstructions when simulation-based priors differ from alternative PSF modeling approaches. The experiment demonstrates consistency under weak supervision, rather than direct correction of unknown residuals in the true on-orbit PSF.

The experiment reveals three fundamental characteristics. First, when trained on labels carrying residuals (PSFEx’s polynomial limitations), these residuals necessarily propagate into the neural network, establishing a performance ceiling bounded by the supervision source. Second, simulation-trained representations provide regularization that stabilizes fine-tuning under noisy supervision, maintaining lower scatter than PSFEx despite noisy labels. Third, any retained features differing from PSFEx could represent either genuine physics (diffraction patterns, inter-CCD correlations) or simulation artifacts. Fine-tuning provides a robust fallback when simulations prove inaccurate, matching traditional methods in their optimal regime.

To surpass this accuracy ceiling, a possible future direction is to adopt an iterative refinement strategy in which simulator parameters are progressively updated using real on-orbit observations. Recent advances in generative modeling have demonstrated the effectiveness of such iterative calibration approaches. For example, Bai et al. (2024) introduced

EMDiffusion, an expectation–maximization framework for training diffusion models from corrupted data, while Barco et al. (2025) and Hosseintabar et al. (2025) explored related iterative updating schemes with improved convergence behavior under misspecified priors. Adapting these ideas to the CSST context would involve treating simulator parameters as learnable quantities that are iteratively refined using residuals between reconstructed PSFs and observed stellar images. In a hierarchical calibration setting, the neural network parameters and simulator parameters could be alternately updated as additional on-orbit data accumulate. Such an approach may provide a pathway toward alleviating the weak-supervision performance ceiling by using real observations as the ultimate constraint rather than intermediate estimators. While beyond the scope of the present work, this direction represents a natural extension of the framework once sufficient on-orbit data becomes available.

### 5.2. Operational Advantages and Broader Implications

While CSST-PSFNet is developed for the CSST imaging survey, several design features make the framework broadly relevant to other space- and ground-based telescopes. The model conditions on focal-plane coordinates and detector identifiers, enabling it to represent both smooth spatial PSF variations and inter-detector discontinuities. This structural flexibility is compatible with a wide range of instruments, including multi-CCD wide-field imagers (e.g., LSST, DECam, Hyper Suprime-Cam) and undersampled space telescopes such as Euclid VIS, Roman WFI, and JWST/NIRCam, where accurate PSF reconstruction is critical for weak-lensing and photometric precision.

However, PSF morphology is fundamentally determined by a telescope’s specific optical and detector design. Consequently, while the architecture of CSST-PSFNet is transferable, the learned parameters are not. Adapting the model to a new instrument would therefore require retraining with that instrument’s own PSF data—either from detailed optical simulations or from on-sky calibration stars. In practice, this adaptation would mainly involve (i) replacing the CSST-specific coordinate and detector embeddings with those reflecting the target focal-plane geometry, and (ii) re-training the network on a modest set of instrument-specific PSFs. The adaptation experiment in Section 5.1, in which the model is updated using weak labels derived from PSFEx, demonstrates that CSST-PSFNet can integrate approximate PSF information effectively, suggesting that only limited calibration data might be necessary for transfer to other instruments.

Looking ahead, data-driven models such as CSST-PSFNet may play an increasingly important role in future instrument calibration pipelines. Traditional calibration strategies, relying on polynomial interpolation, sparse calibration stars, or static optical models, may become insufficient as surveys demand higher resolution, tighter stability, and stricter control of weak-lensing residuals. A generative PSF model that can merge simulation data, laboratory measurements, and on-orbit observations offers a more flexible alternative.

In a future calibration architecture, a deep PSF model could serve as a continuously updated representation of the instrument’s optical state. The network could be initialized with pre-launch simulations and refined progressively using commissioning data, approximate PSF estimates, or dedicated calibration fields. The conditioning strategy further enables the inclusion of temporal or environmental metadata—such as orbital temperature, alignment sensors, or attitude-control diagnostics—thereby potentially enabling the construction of time-dependent PSF models.

## 6. CONCLUSIONS

In this work, we introduced CSST-PSFNet, a deep-learning framework for high-fidelity PSF reconstruction, specifically designed for the CSST. By integrating convolutional feature extraction, Transformer-based global aggregation, and variational latent modeling, the network effectively captures both local PSF structures and large-scale variations across the multi-CCD focal plane. The incorporation of geometric coordinate encoding and CCD-specific embeddings further enables the model to represent spatially varying, detector-dependent PSF behavior in a unified manner.

Using high-resolution simulated star–PSF pairs generated by the CSST Main Survey Simulator, CSST-PSFNet achieves improved pixel-level accuracy and more precise recovery of weak-lensing–sensitive shape parameters compared to the widely used PSFEx algorithm under the simulated conditions considered in this study. The model further demonstrates stable performance within the tested Gaussian-blur perturbation regime, indicating robustness to moderate, controlled deviations from the nominal PSF morphology.

To assess the applicability of the model under realistic on-orbit conditions, we further performed an adaptation test in which the ground truth PSF is assumed unavailable, and PSFs estimated by PSFEx serve as weak supervision. Through limited fine-tuning, the model aligns with PSFEx-level reconstruction accuracy while maintaining reduced statistical scatter. This result demonstrates consistency under weak supervision rather than direct correction of

unknown residuals, and suggests that the framework can flexibly incorporate approximate PSF information when high-fidelity supervision is not accessible.

We emphasize that the present validation is performed within a high-fidelity simulation regime. Full assessment under operational conditions will require real on-orbit observations, including multi-epoch calibration stars and time-dependent instrument monitoring. With such data, hierarchical or iterative calibration strategies may further refine the physical consistency of the model. Within its current scope, CSST-PSFNet provides a scalable and instrument-aware approach to PSF reconstruction for undersampled, wide-field space imaging surveys such as CSST.

#### DATA AVAILABILITY

The simulated datasets used in this study were generated using the CSST Main Survey Simulator (`csst_msc_sim`) within the CSST collaboration framework. Due to the large data volume and the dependence on internal simulation components and configurations of the CSST project, the processed datasets and trained model weights cannot be publicly deposited at present. The core model implementation and data-processing framework are publicly available via the authors' GitHub repository. However, full reproduction of the datasets requires access to internal CSST simulation resources and configurations that are not currently publicly accessible. The simulation configurations and methodological details described in Section 2 document the data-generation procedure and workflow. Access to the processed datasets and trained model weights may be granted by the corresponding author upon reasonable request and subject to collaboration approval.

#### ACKNOWLEDGMENTS

This work is based in part on the software created by the CSST Simulation Team, which is supported by the CSST scientific data processing and analysis system of the China Manned Space Project. The authors acknowledge support by the CSST Scientific Data Processing System (No. CMS-CSST-2025-A11), the China National Science Foundation (NSFC) (Nos. 12433012, 12373097), the China Manned Space Project (grant Nos. CMS-CSST-2025-A19, CMS-CSST-2025-A21), and the National Astronomical Observatories, Chinese Academy of Sciences (Project No. E4ZR050901).

#### REFERENCES

- Akeson, R., Armus, L., Bachelet, E., et al. 2019, The Wide Field Infrared Survey Telescope: 100 Hubbles for the 2020s. <https://arxiv.org/abs/1902.05569>
- Anderson, J., & King, I. R. 2000, Publications of the Astronomical Society of the Pacific, 112, 1360, doi: [10.1086/316632](https://doi.org/10.1086/316632)
- Anderson, J., & King, I. R. 2006, PSFs, Photometry, and Astronomy for the ACS/WFC, Instrument Science Report ACS 2006-01, 34 pages
- Avanaki, A. 2009, OPTICAL REVIEW, 16, 613–621, doi: <https://doi.org/10.1007/s10043-009-0119-z>
- Bai, W., Wang, Y., Chen, W., & Sun, H. 2024, arXiv e-prints, arXiv:2407.01014, doi: [10.48550/arXiv.2407.01014](https://doi.org/10.48550/arXiv.2407.01014)
- Bai, Z., Jia, P., Lv, J., et al. 2025, An Ultra-Fast Image Simulation Technique with Spatially Variable Point Spread Functions. <https://arxiv.org/abs/2502.10015>
- Ban, Z., Li, X., Yang, X., & Jiang, Y. 2022, Journal of System Simulation, 34, doi: <https://doi.org/10.16182/j.issn1004731x.joss.21-0582>
- Ban, Z., Li, X.-B., Yang, X., et al. 2025, Mock Observations for the CSST Mission: End-to-End Performance Modeling of Optical System. <https://arxiv.org/abs/2511.06936>
- Barco, G. M., Adam, A., Stone, C., Hezaveh, Y., & Perreault-Levasseur, L. 2025, ApJ, 980, 108, doi: [10.3847/1538-4357/ad9b92](https://doi.org/10.3847/1538-4357/ad9b92)
- Bartelmann, M., & Schneider, P. 2001, Physics Reports, 340, 291–472, doi: [10.1016/s0370-1573\(00\)00082-x](https://doi.org/10.1016/s0370-1573(00)00082-x)
- Bergamini, P., Acebron, A., Grillo, C., et al. 2023, The Astrophysical Journal, 952, 84, doi: [10.3847/1538-4357/acd643](https://doi.org/10.3847/1538-4357/acd643)
- Bertin, E. 2011, in Astronomical Society of the Pacific Conference Series, Vol. 442, Astronomical Data Analysis Software and Systems XX, ed. I. N. Evans, A. Accomazzi, D. J. Mink, & A. H. Rots, 435
- Bertin, E., & Arnouts, S. 1996, A&AS, 117, 393, doi: [10.1051/aas:1996164](https://doi.org/10.1051/aas:1996164)
- Cao, Y., Gong, Y., Meng, X.-M., et al. 2018, Monthly Notices of the Royal Astronomical Society, doi: [10.1093/mnras/sty1980](https://doi.org/10.1093/mnras/sty1980)

- Carney, J., Corbett, H., Marshall, W., et al. 2024, in *Software and Cyberinfrastructure for Astronomy VIII*, ed. J. Ibsen & G. Chiozzi, Vol. 13101, International Society for Optics and Photonics (SPIE), 131010O, doi: [10.1117/12.3020465](https://doi.org/10.1117/12.3020465)
- Collaboration, C., Gong, Y., Miao, H., et al. 2025, *Introduction to the Chinese Space Station Survey Telescope (CSST)*. <https://arxiv.org/abs/2507.04618>
- Gong, Y., Liu, X., Cao, Y., et al. 2019, *The Astrophysical Journal*, 883, 203, doi: [10.3847/1538-4357/ab391e](https://doi.org/10.3847/1538-4357/ab391e)
- Gong, Y., et al. 2025, *Sci. China Phys. Mech. Astron.*, 68, 280402, doi: [10.1007/s11433-025-2646-2](https://doi.org/10.1007/s11433-025-2646-2)
- Guinot, A., Kilbinger, M., Farrens, S., et al. 2022, *Astronomy & Astrophysics*, 666, A162, doi: [10.1051/0004-6361/202141847](https://doi.org/10.1051/0004-6361/202141847)
- Heymans, C., Brown, M. L., Barden, M., et al. 2005, *Monthly Notices of the Royal Astronomical Society*, 361, 160, doi: [10.1111/j.1365-2966.2005.09152.x](https://doi.org/10.1111/j.1365-2966.2005.09152.x)
- Hirata, C., & Seljak, U. 2003, *Monthly Notices of the Royal Astronomical Society*, 343, 459, doi: [10.1046/j.1365-8711.2003.06683.x](https://doi.org/10.1046/j.1365-8711.2003.06683.x)
- Hosseintabar, D., Chen, F., Daras, G., Torralba, A., & Daskalakis, C. 2025, arXiv e-prints, arXiv:2510.12691, doi: [10.48550/arXiv.2510.12691](https://doi.org/10.48550/arXiv.2510.12691)
- Jia, P., Wu, X., Li, Z., et al. 2021, *Monthly Notices of the Royal Astronomical Society*, 505, 4717–4725, doi: [10.1093/mnras/stab1461](https://doi.org/10.1093/mnras/stab1461)
- Jia, P., Wu, X., Yi, H., Cai, B., & Cai, D. 2020, *The Astronomical Journal*, 159, 183, doi: [10.3847/1538-3881/ab7b79](https://doi.org/10.3847/1538-3881/ab7b79)
- Kaiser, N., Squires, G., & Broadhurst, T. 1995, *The Astrophysical Journal*, 449, 460, doi: [10.1086/176071](https://doi.org/10.1086/176071)
- Krist, J. 1993, in *Astronomical Society of the Pacific Conference Series*, Vol. 52, *Astronomical Data Analysis Software and Systems II*, ed. R. J. Hanisch, R. J. V. Brissenden, & J. Barnes, 536
- Lanusse, F., Mandelbaum, R., Ravanbakhsh, S., et al. 2021, *Monthly Notices of the Royal Astronomical Society*, 504, 5543, doi: [10.1093/mnras/stab1214](https://doi.org/10.1093/mnras/stab1214)
- Liaudat, T., Starck, J.-L., Kilbinger, M., & Frugier, P.-A. 2023, *Inverse Problems*, 39, 035008, doi: [10.1088/1361-6420/acb664](https://doi.org/10.1088/1361-6420/acb664)
- Ling, C., Ren, J., Shao, L., et al. 2026, *Selecting Optimal Stellar Calibration Fields for the CSST Imaging Survey*. <https://arxiv.org/abs/2602.11864>
- Mandelbaum, R., Miyatake, H., Hamana, T., et al. 2017, *Publications of the Astronomical Society of Japan*, 70, S25, doi: [10.1093/pasj/psx130](https://doi.org/10.1093/pasj/psx130)
- Mellier, Y., Abdurro'uf, Acevedo Barroso, J. A., et al. 2025, *Astronomy & Astrophysics*, 697, A1, doi: [10.1051/0004-6361/202450810](https://doi.org/10.1051/0004-6361/202450810)
- Ngolè, F., Starck, J.-L., Okumura, K., Amiaux, J., & Hudelot, P. 2016, *Inverse Problems*, 32, 124001, doi: [10.1088/0266-5611/32/12/124001](https://doi.org/10.1088/0266-5611/32/12/124001)
- Ni, S., Qiu, Y., Chen, Y., et al. 2024, *PI-AstroDeconv: A Physics-Informed Unsupervised Learning Method for Astronomical Image Deconvolution*. <https://arxiv.org/abs/2403.01692>
- Nie, J., Wei, P., Cao, Z., et al. 2025, *Toward High-Precision Astrometry with CSST Using Multi-Gaussian Fitting of PSF*. <https://arxiv.org/abs/2508.10329>
- Paris, D., Merlin, E., Fontana, A., et al. 2023, *The Astrophysical Journal*, 952, 20, doi: [10.3847/1538-4357/acda8a](https://doi.org/10.3847/1538-4357/acda8a)
- Paulin-Henriksson, S., Amara, A., Voigt, L., Refregier, A., & Bridle, S. L. 2008, *Astronomy & Astrophysics*, 484, 67–77, doi: [10.1051/0004-6361:20079150](https://doi.org/10.1051/0004-6361:20079150)
- Paulin-Henriksson, S., Refregier, A., & Amara, A. 2009, *Astronomy & Astrophysics*, 500, 647–655, doi: [10.1051/0004-6361/200811061](https://doi.org/10.1051/0004-6361/200811061)
- Rowe, B. T. P., Jarvis, M., Mandelbaum, R., et al. 2015, *Astronomy and Computing*, 10, 121, doi: [10.1016/j.ascom.2015.02.002](https://doi.org/10.1016/j.ascom.2015.02.002)
- Spergel, D., Gehrels, N., Baltay, C., et al. 2015, *Wide-Field Infrared Survey Telescope-Astrophysics Focused Telescope Assets WFIRST-AFTA 2015 Report*. <https://arxiv.org/abs/1503.03757>
- Treu, T., Roberts-Borsani, G., Bradac, M., et al. 2022, *The Astrophysical Journal*, 935, 110, doi: [10.3847/1538-4357/ac8158](https://doi.org/10.3847/1538-4357/ac8158)
- Wang, Z., Bovik, A., Sheikh, H., & Simoncelli, E. 2004, *IEEE Transactions on Image Processing*, 13, 600, doi: [10.1109/TIP.2003.819861](https://doi.org/10.1109/TIP.2003.819861)
- Wei, C.-L., Li, G.-L., Fang, Y.-D., et al. 2025, *Mock Observations for the CSST Mission: Main Surveys—An Overview of Framework and Simulation Suite*. <https://arxiv.org/abs/2511.06970>
- Zhan, H. 2021, *Kexue Tongbao/Chinese Science Bulletin*, 66, 1290–1298, doi: [10.1360/TB-2021-0016](https://doi.org/10.1360/TB-2021-0016)
- Zuntz, J., Sheldon, E., Samuroff, S., et al. 2018, *Monthly Notices of the Royal Astronomical Society*, 481, 1149–1182, doi: [10.1093/mnras/sty2219](https://doi.org/10.1093/mnras/sty2219)